Commun. Comput. Phys.
doi: 10.4208/cicp.OA-2021-0131

Vol. **x**, No. x, pp. 1-19
xxx 20xx

Mesh Adaptation for Curing the Pathological Behaviors of an Upwind Scheme

Yifan Xia[1], Jianjing Zheng[2,*], Jianfeng Zhou[1], Jifa Zhang[1], Gaofeng Wang[1] and Yao Zheng[1]

[1] *School of Aeronautics and Astronautics, Zhejiang University, Hangzhou 310027, P.R. China.*
[2] *Center for Hypergravity Experimental and Interdisciplinary Research, Zhejiang University, Hangzhou 310027, P.R. China.*

Communicated by Michael Dumbser

Received 18 June 2021; Accepted (in revised version) 13 November 2021

Abstract. In present paper, mesh adaptation is applied for curing the pathological behaviors of the enhanced time-accurate upwind scheme (Loh & Jorgenson, AIAAJ 2016). In the original ETAU (enhanced time-accurate upwind) scheme, a multi-dimensional dissipation model is required to cure the pathological behaviors. The multi-dimensional dissipation model will increase the global dissipation level reducing numerical resolution. In present work, the metric-based mesh adaptation strategy provides an alternative way to cure the pathological behaviors of the shock capturing. The Hessian matrix of flow variables is applied to construct the metric, which represents the curvature of the physical solution. The adapting operation can well refine the anisotropic meshes at the location with large gradients. The numerical results show that the adaptation of mesh provides a possible way to cure the pathological behaviors of upwind schemes.

AMS subject classifications: 65M08, 65M12, 65M55

Key words: Metric tensor, mesh adaptation, finite volume scheme, unstructured grid.

1 Introduction

For finite volume methods, upwind schemes are very popular due to their robustness and geometric flexibility. Following Godunov's idea [1], the Godunov type upwind schemes

*Corresponding author. *Email addresses:* xiayifan@zju.edu.cn (Y. Xia), zhengjianjing@zju.edu.cn (J. Zheng), zoujianfeng@zju.edu.cn (J. Zou), jfzhang@zju.edu.cn (J. Wang), gfwang@zju.edu.cn (G. Wang), yao.zheng@zju.edu.cn (Y. Zheng)

[2–4] applied a Riemann solver for flux calculations. However, they contain some cases of pathological behaviors, including the carbuncle phenomenon, the kinked Mach stem, the expansion shock and the numerical oscillation across a slow moving shock etc. [5–7].

The most renowned pathological behavior is the carbuncle phenomenon. It is firstly observed by Peery and Imlay [6]. The carbuncle phenomenon refers unphysical solutions at the stagnation region for computation of a supersonic flow over a blunt body. Many efforts have being made to study the origin of the carbuncle phenomenon. Through linear analysis, Sanders et al. [8] suggested the anomaly is the result of inadequate cross flow dissipation. Robinet et al. [9] pointed out that the carbuncle phenomenon is linked to the intrinsic instability of the Euler equations. By linear stability analysis, Gressier et al. [10] suggested the odd-even decoupling contributes the failures in some situations. By matrix stability analysis, Dumbser et al. [11] confirmed the problem of the odd-even decoupling. According to Xu et al. [12, 13], the dissipative mechanism of Godnov-type schemes is mainly from the averaging stage. In the direction parallel to the normal shock, the velocity is almost the same for two neighboring mesh cells, the numerical dissipation introduced in the averaging process diminishes. Without enough dissipation, the perturbation of pressure field will feed the density field, which is likely to induce shock instability. Kemm [14] also identified that low numerical viscosity on shear waves is the source of carbuncle. It is generally agreed that the insufficient dissipation is responsible for the pathological behaviors. Various methods have been proposed to cure the pathological behaviors. For instance, Quirk [7] used a more dissipative HLLE scheme near the shock. Lin [15] proposed a cure of Roe's scheme by reducing second-order accuracy to first-order accuracy inside the shock layer. Kim et al. [16] proposed a function to control the damping characteristic of Roe's scheme. Loh and Jorgenson [17] proposed a multi-dimensional dissipation model to systematic cure the pathological behaviors. However, these approaches will increase the dissipation level, thus reducing the numerical resolution, increasing the shock thickness or smearing some features of the flow field. Recently, Fleischmann et al. [18, 19] proposed a novel approach that cures the carbuncle phenomenon by reducing numerical dissipation instead of increasing it. They suggested that the inadequate scaling of the acoustic dissipation in the low Mach number limit causes the instability. By modifying the eigenvalue calculation in the Roe approximation, the approach can prevent the grid-aligned shock instability.

On the other hand, according to Quirk's observation [7], the alignment of the grid line to the shock is an essential condition for triggering the pathological behaviors. Meanwhile, Pandolfi and D'Ambrosio [20] proposed that the grid aspect ratio has significant influence to the carbuncle phenomenon. The elongated elements along the normal of the shock promote the instabilities, whereas elements stretched along the tangent to the shock have a damping effect. Recently, Rodionov [21] suggested that the grid alignment with the flow lines at the shock front is critical for the activation of the physical anomaly. He also pointed out that the numerical instability is sensitive to the size and shape of the grid cells.

These works inspired us to cure the pathological behaviors from the aspect of mesh

adaptation. In computational aerodynamics, mesh adaptation is an effective way for capturing complicate physical features. Numerous papers have been published dealing with mesh adaptation for numerical simulations. [22–27] The unstructured and anisotropic mesh adaptation method is very popular and effective, which is realized by mesh operation based on a predefined manner.

The metric-based mesh adaptation was introduced in the pioneering works of Diaz and Hecht [25, 26] in 1997. It is able to transform any unstructured isotropic mesh generator into an anisotropic one. This is done by computing the distance in a Riemannian metric space instead of the classical Euclidean one. Then, the adaptive mesh generator creates a unit-mesh in the Riemannian metric space. There are many beneficial impacts of the mesh adaptation operation. It can not only reduce the amount of required mesh elements, but also better resolve the multi-scale features of flow fields. Especially, the mesh adaptation strategy has a natural advantage of shock capture, because most adaptation algorithms are based on the gradient of flow variables. The shock resolution can be significantly improved by mesh refinement across the interface with sharp jump of physical variables. Furthermore, the anisotropic property across the shock layer of the anisotropic mesh can damp the shock instability.

Thus, it is possible to use the anisotropic mesh adaptation strategy to better resolve the shock and cure the pathological behaviors of upwind finite volume methods on unstructured grids. In present work, a metric-based mesh adaptation algorithm is applied to cure the pathological behaviors of the original ETAU scheme. The metric is constructed based on the Hessian matrix of the flow variable. It can well refine the mesh resolution at the location with large gradients, thus shocks. Meanwhile, the anisotropic property of the cells in the shock layer has a damping effect of the numerical instability. The basic finite volume solver applied is the enhanced time-accurate upwind scheme (ETAU) [28, 29].

2 Fundamentals of the enhanced time-accurate upwind scheme

The basic flow solver for the compressible Euler and Navier-Stokes equations is the enhanced time-accurate upwind scheme [29, 30]. The ETAU scheme has been proven to be very robust for a wide range of compressible flows, which is second order in space and time [28, 29].

2.1 Conservation form of the compressible Euler and Navier-Stokes equations

The two dimensional Euler and Navier-Stokes equations can be written in the following vector form as

$$U_t + F_x + G_y = 0, \tag{2.1}$$

where x, y and t are the streamwise, transverse and time coordinates, respectively. Generally, the flux vectors $\boldsymbol{F}$ and $\boldsymbol{G}$ are split into inviscid and viscous parts:

$$F=F_i-F_v,\quad G=G_i-G_v.$$

The conservative flow variable vector $\boldsymbol{U}$ and the inviscid flux vectors $\boldsymbol{F_i}$ and $\boldsymbol{G_i}$ are given in non-dimensional forms as

$$U=\begin{pmatrix}U_1\\U_2\\U_3\\U_4\end{pmatrix}=\begin{pmatrix}\rho\\\rho u\\\rho v\\\rho e\end{pmatrix},\quad F_i=\begin{pmatrix}\rho u\\\rho u^2+p\\\rho uv\\\rho uH\end{pmatrix},\quad G_i=\begin{pmatrix}\rho v\\\rho uv\\\rho v^2+p\\\rho vH\end{pmatrix}. \tag{2.2}$$

Respectively, ρ, u, v, and p are the density, two velocity components, and static pressure. Let γ be the constant specific heat ratio. The total energy can be expressed as

$$e=\frac{p}{\rho(\gamma-1)}+\frac{1}{2}(u^2+v^2),$$

and the total enthalpy is $H=p/\rho+e$.

The non-dimensional viscous flux vectors $\boldsymbol{F_v}$ and $\boldsymbol{G_v}$ are written in conservation forms as

$$F_v=\begin{pmatrix}0\\\mu(2u_x-\frac{2}{3}\nabla\cdot V)\\\mu(v_x+u_y)\\\mu[(2uu_x+(u_y+v_x)v-\frac{2}{3}(\nabla\cdot V)u+\frac{\gamma}{Pr}\frac{\partial}{\partial x}(\frac{U_4}{U_1}-\frac{u^2+v^2}{2})]\end{pmatrix} \tag{2.3}$$

and

$$G_v=\begin{pmatrix}0\\\mu(v_x+u_y)\\\mu(2v_y-\frac{2}{3}\nabla\cdot V)\\\mu[(2vv_x+(u_y+v_x)u-\frac{2}{3}(\nabla\cdot V)v+\frac{\gamma}{Pr}\frac{\partial}{\partial y}(\frac{U_4}{U_1}-\frac{u^2+v^2}{2})]\end{pmatrix}, \tag{2.4}$$

where u_x, u_y, v_y and v_y are the flow velocity gradients with $\boldsymbol{Pr}$ being the Prandtl number. $\mu=1/Re$ is the dynamic viscosity coefficient, where $\boldsymbol{Re}$ is the Reynolds number; and the velocity divergence is $\nabla\cdot V=u_x+v_y$. For air at standard condition, there is $\gamma=1.4$; and the Prandtl number is $Pr=0.72$.

For finite volume scheme, the Gauss divergence theorem is applied to the control volume. As depicted in Fig. 1, $\Delta\mathbf{ABC}$ is the control volume, in a typical 2D unstructured triangular grid. The unstructured grid is a natural environment for the incorporation of mesh adaptation algorithms. The quadrature of surface integrals leads to the discretized form of the ETAU scheme:

$$U^{n+1}=U^n-\frac{\Delta t}{\Delta s}\sum_{k=1}^{3}[F_k^{n+1/2}(n_x)_k+G_k^{n+1/2}(n_y)_k]\Delta l_k\,, \tag{2.5}$$

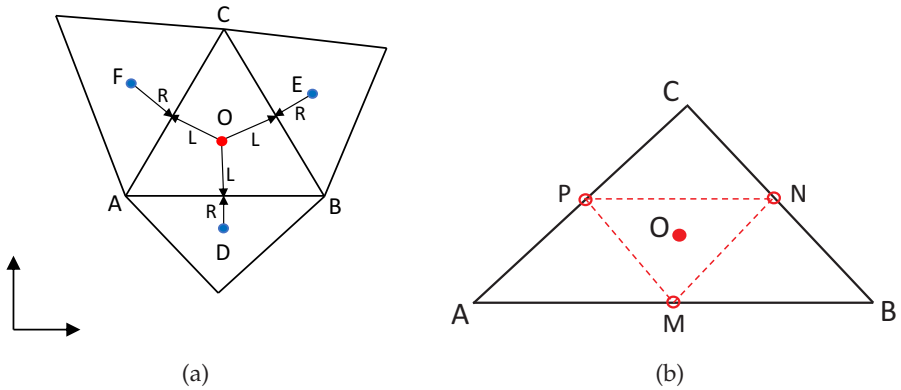

(a) (b)

Figure 1: The illustration of (a) the control volume in a typical unstructured triangular grid with left and right state of each edge; (b) **M**,**N**, **P** are the cell edge centers.

where U^n and U^{n+1} are the cell average values at current and next time level, respectively. Δt is the time step. The flow variables are stored at the triangle cell centers. The area of control volume denotes as Δs and the length of each edge is Δl_k. Meanwhile, $(n_x,n_y)_k$ is the outgoing normal vector of each edge.

2.2 Variable reconstruction and the multidimensional limiting

The cell average-flow variables are reconstructed into second-order polynomials within the control volume. The evaluation of spatial gradients and time derivatives is a critical step. As shown in Fig. 1, the flow data $\boldsymbol{U}$ is stored at current cell center **O** and its three neighboring cell centers **D**, **E**, and **F**. Let u be a component of $\boldsymbol{U}$. By simple finite difference, three linear equations for the gradients give as:

$$\begin{aligned}(x_D-x_O)u_x+(y_D-y_O)u_y&=u_D-u_O,\\(x_E-x_O)u_x+(y_E-y_O)u_y&=u_E-u_O,\\(x_F-x_O)u_x+(y_F-y_O)u_y&=u_F-u_O.\end{aligned}\tag{2.6}$$

The subscripts **O**, **D**, **E**, and **F** denote the corresponding cell centers. Any combination of two of these equations yields a set of spatial gradients for u, namely (u_x^i,u_y^i) $(i=1,2,3)$. Their moduli gives as

$$m_i=\sqrt{\left[u_x^{(i)}\right]^2+\left[u_y^{(i)}\right]^2},\quad i=1,2,3.\tag{2.7}$$

Two limiters are recommended, thus the minmod limiter and the extended van Albada limiter [31]. When the minmod limiter is applied, the gradients (u_x^i,u_y^i) are corresponding to $m_i=\min(m_1,m_2,m_3)$. Generally, the minmod limiter can work well. For cases with strong discontinuity, the van Albada limiter is employed, which is a weighted averaging. Three weights are defined as

$$\omega_1=(m_2m_3)^\alpha,\quad \omega_2=(m_1m_3)^\alpha,\quad \omega_3=(m_1m_2)^\alpha.\tag{2.8}$$

Then, the limited gradients are evaluated as

$$u_x = \frac{\omega_1 u_x^{(1)} + \omega_2 u_x^{(2)} + \omega_3 u_x^{(3)}}{\omega_1 + \omega_2 + \omega_3}, \quad u_y = \frac{\omega_1 u_y^{(1)} + \omega_2 u_y^{(2)} + \omega_3 u_y^{(3)}}{\omega_1 + \omega_2 + \omega_3}. \tag{2.9}$$

The free parameter $\alpha \geq 0$ provides some numerical dissipation. A small α (e.g. $\alpha = 0.5$) usually gives less dissipation. For extreme situations with strong discontinuity, like the presence of shocks, a large value of α (e.g. $\alpha = 2.0$) is needed.

After the spatial gradients U_x^n, U_y^n are obtained, the Cauchy-Kowalewski concept is used to calculate the time derivative U_t, by using the governing equations to represent the time derivative by the spatial derivatives. This idea was first used in the Lax-Wendroff scheme and also employed by the NT [32] and CE/SE schemes [33]. Following this concept, the time derivative is given as

$$U_t^n = -F_x^n - G_y^n. \tag{2.10}$$

As Reynolds number **Re** is usually high (or viscosity μ is small), the fluxes $\boldsymbol{F}$ and $\boldsymbol{G}$ can be well approximated by their inviscid portions:

$$U_t^n = -\left(\frac{\partial F_i}{\partial U}\right)^n U_x^n - \left(\frac{\partial G_i}{\partial U}\right)^n U_y^n. \tag{2.11}$$

After the spatial gradients and time derivatives have been obtained, **L**(left) and **R**(right) states of each edges of the control volume can be given. Then, the inviscid fluxes are calculated by a Riemann Solver [2]. The Riemann solver can compromise the two different states across the cell interface, with the values of the **L**(left) and **R**(right) states. On the other hand, the viscous fluxes are calculated by the Right-state.

Note that, when the Gauss divergence theorem is applied, only the flow variables normal to the interface are considered. The components parallel to the cell interface are ignored with no control. Meanwhile, when the cell interface flux is calculated with a Riemann solver, only the flow variables normal to the interface are considered. Their components parallel to the interface are completely ignored with no control or damping (see e.g. [17]). This is the reason why the pathological behaviors often happen in upwind schemes. For example, assume a cell interface lies along with the shock, then the numerical solution is vulnerable to any disturbance/instabilities in the direction aligned with the shock, causing the carbuncle phenomena. Certain dissipation should be added to suppress such anomaly. In the previous ETAU scheme, a multi-dimensional dissipation model is developed to systematically cure the pathological behaviors.

2.3 Multi-dimensional dissipation model

The ETAU scheme is an improved upwind scheme of Godunov type. The Godunov type methods contains subtle flaws of the so-called pathological behaviors. In the original

ETAU scheme, a multidimensional dissipation model [17] is applied to cure the pathological behaviors. This distinctive method is based on increasing the dissipation by averaging the conservative variables at each time step.

Shown in Fig. 1(b), **M**, **N** and **P** are the midpoints of the edge **AB**, **BC**, and **CA**. The right state at these midpoints are extrapolated from their neighboring cell centers **D**, **E** and **F** by using Taylor expansion:

$$\begin{aligned} U_M^n &= U_D^n + (U_x^n)_D \Delta x + (U_y^n)_D \Delta y, \\ U_N^n &= U_E^n + (U_x^n)_E \Delta x + (U_y^n)_E \Delta y, \\ U_P^n &= U_F^n + (U_x^n)_F \Delta x + (U_y^n)_F \Delta y. \end{aligned} \tag{2.12}$$

The average of these values are given by

$$\tilde{U} = (U_M^n + U_N^n + U_P^n)/3. \tag{2.13}$$

Here $\tilde{U}$ is an approximation of U_o with some spatial smearing at each time step. The multi-dimensional dissipation model is realized by replacing U^n with a weighted average $(\beta\tilde{U} + (1-\beta)U^n)$, which induces some omni-directional dissipation. Then, the ETAU scheme [28–30] is given as

$$U^{n+1} = \beta\tilde{U} + (1-\beta)U^n - \frac{\Delta t}{\Delta s}\sum_{k=1}^{3}[F_k^{n+1/2}(n_x)_k + G_k^{n+1/2}(n_y)_k]\Delta l_k, \tag{2.14}$$

where $\beta > 0$ is the weighing factor, which controls level of the numerical dissipation.

By this weighted averaging process, some numerical dissipation is introduced to the scheme. Most subsonic or low supersonic flows are insensitive to this weighing factor, while $\beta = 0.001$ is enough. For flows with high Mach number, β may need to increase to 0.1. This dissipation method is very versatile, because it is external to the Riemann solver. The numerical results [28,29] showed that it can systematically cure the pathological behaviors. However, it will globally increase the dissipation. This may smear some features of the flow field. Meanwhile, the weighting factor is varied to fit a specific case.

3 Metric-based mesh adaptation

In present work, a metric-based mesh adaptation algorithm is employed to resolve the presence of shocks and alleviate its instabilities. The main strategy of anisotropic mesh adaptation is based on Riemannian metric tensors [34–36]. Then, the requirements on the mesh for sizes, shapes and orientations are expressed in term of a metric tensor field. In order to clearly express the method, some basic concepts of metric tensor are briefed in following.

3.1 Basic concept of metric tensor

A metric tensor field of domain Ω is a Riemannian metric space, which can be denoted by $(\mathscr{M}(x))_{x\in\Omega}$. A metric tensor $\mathscr{M}$ in space $\mathbb{R}^n$ is an $n\times n$ symmetric definite positive matrix. Thus, $\mathscr{M}$ is always diagonalizable and can be decomposed as

$$\mathscr{M} = {}^t\mathcal{R}\Lambda\mathcal{R}, \tag{3.1}$$

where $\mathcal{R}$ and Λ are the eigenvectors and the eigenvalues, respectively. Here, Λ is a diagonal matrix, composed by positive eigenvalues λ; and $\mathcal{R}$ is a orthonormal matrix, there is $\mathcal{R}^t = \mathcal{R}^{-1}$.

The scalar product of two vectors in space $\mathbb{R}^n$ can be defined related to a metric $\mathscr{M}$ as

$$<\mathbf{u},\mathscr{M}\mathbf{v}>, \tag{3.2}$$

where the natural dot product of $\mathbb{R}^n$ has been denoted by $<\mathbf{u},\mathbf{v}>$. Under this notion, the Euclidean norm of a vector $\mathbf{u}$ in $\mathbb{R}^n$ according to the metric $\mathscr{M}$, is defined as

$$\|\mathbf{u}\|_{\mathscr{M}} = \sqrt{\langle\mathbf{u},\mathbf{u}\rangle_{\mathscr{M}}} = \sqrt{{}^t\mathbf{u}\mathscr{M}\mathbf{u}}. \tag{3.3}$$

This norm measures the length of vector $\mathbf{u}$ with respect to the metric $\mathscr{M}$.

The computation of lengths and volumes are two fundamental geometric operation in a mesh generator. The length of edges in the adaptive mesh are calculated in the Riemannian metric space, rather than in the Euclidean one. Assume the end points of an edge are $\mathbf{x_i}$ and $\mathbf{x_j}$, the edge $\mathbf{e} = [x_i, x_j]$ can be expressed using the parameterization $\gamma(t) = \mathbf{x_i} + t\mathbf{e}$, $t\in[0,1]$. Then, the length of the edge $\mathbf{e}$ can be computed as

$$\ell_{\mathcal{M}}(\mathbf{e}) = \int_0^1 \sqrt{{}^t\mathbf{e}\mathcal{M}(\mathbf{x}_i + t\mathbf{e})\mathbf{e}}\mathrm{d}t. \tag{3.4}$$

The volume of an element K is evaluated by

$$|K|_{\mathcal{M}} = \int_K \sqrt{\det(\mathcal{M}(\mathbf{x}))}\mathrm{d}\mathbf{x}. \tag{3.5}$$

The basic idea of metric-based mesh adaption is very simple, but practical. Now, for metric-based mesh adaptation, the key step is the construction of the metric tensor field.

3.2 Construction of metric tensor

The computation of the metric is obviously the central point for the metric-based mesh adaptation. Given a discrete numerical solution on a 2D grid, an Hessian matrix $\mathcal{H}$ of a flow variable (ϕ_h) at the node of the computational mesh, is the matrix of second derivatives, written as

$$\mathcal{H} = \begin{bmatrix} \frac{\partial^2\phi_h}{\partial x^2} & \frac{\partial^2\phi_h}{\partial x\partial y} \\ \frac{\partial^2\phi_h}{\partial y\partial x} & \frac{\partial^2\phi_h}{\partial y^2} \end{bmatrix}. \tag{3.6}$$

The physical meaning of the Hessian matrix is the curvature of the solution's map. It is reasonable to place more mesh cells where the curvature is large. Then, defining the metric based on the Hessian matrix is a natural idea.

Obviously, the Hessian matrix $\mathcal{H}$ is symmetric and can be decomposed as

$$\mathcal{H} = {}^t\mathcal{R}\Lambda\mathcal{R} = \begin{bmatrix} \vec{e}_1 & \vec{e}_2 \end{bmatrix} \begin{bmatrix} \lambda_1 & 0 \\ 0 & \lambda_2 \end{bmatrix} \begin{bmatrix} \vec{e}_1^T \\ \vec{e}_2^T \end{bmatrix}, \tag{3.7}$$

where $\vec{e}_i$ are the eigenvectors, and λ_i are the eigenvalues. In practice, the Hessian matrix should be slightly modified in order to construct the adaptation metric, which is given as

$$\mathcal{M} = {}^t\mathcal{R}\tilde{\Lambda}\mathcal{R} = \begin{bmatrix} \vec{e}_1 & \vec{e}_2 \end{bmatrix} \begin{bmatrix} \tilde{\lambda}_1 & 0 \\ 0 & \tilde{\lambda}_2 \end{bmatrix} \begin{bmatrix} \vec{e}_1^T \\ \vec{e}_2^T \end{bmatrix}, \tag{3.8}$$

where

$$\tilde{\lambda}_i = \min\left(\max\left(c|\lambda_i|/\epsilon, h_{\max}^{-2}\right), h_{\min}^{-2}\right).$$

This presents the metric computation based on the Hessian matrix. During remeshing process, the target size along the direction of the eigenvector $\vec{e}_1$ is $h_i = \tilde{\lambda}_i^{-1/2}$. The values of the free parameters $h_{\min}$ and $h_{\max}$ are user defined, which denote the minimum and maximum allowable target edge sizes, while the constant c/ϵ controls the level of interpolation error and consequently the final number of mesh elements.

In present work, the open source package Mmg [36] is applied to adapt the mesh. This package can generate an anisotropic mesh complying with the prescribed metric M_i and user defined parameters, with the local mesh operators, including points insertion, swaps of edges and points smoothing.

As we have discussed, the reason why the pathological behaviors often happen in upwind schemes is that when the cell interface flux is calculated with a Riemann solver, only the flow variables normal to the interface are considered. Their components parallel to the interface are completely ignored with no damping. This operation in the upwind schemes makes the numerical solution is vulnerable to the disturbance in the direction aligned with the shock, causing the carbuncle phenomena. Hence, certain dissipation mechanism should be added to suppress such anomaly. As we proposed in this paper, one way to do so is to use elongated mesh in the direction parallel to the shock. As numerically, a larger mesh size or elongation in this direction implies more numerical dissipation.

With the presence of shock, the gradients of flow variables are very large, especially in the direction normal to the shock. Meanwhile, the gradients in the direction parallel to the shock are relatively small compared to the normal direction. During the remeshing process, the Hessian matrix of the flow variable has a large value normal to the shock, and a small value parallel to the shock. Thus, the meshes adapted by the Hessian-based metric have the stretch effect in the direction parallel to the shock. A larger mesh size will be achieved in the direction parallel to the shock. This means more dissipation in the parallel direction is added, which is beneficial for the damping of shock instability.

4 Numerical results and discussion

(a) Supersonic flow past a cylinder

The first example is the supersonic flow past a cylinder. A freestream of $Ma = 10.0$ is imposed at the inlet boundary. The matched layer-capturing absorbing boundary condition [39] is applied to the outflow boundary. At the cylinder, the slip wall condition is applied. For upwind schemes, the bow shock is prone to be instable at the stagnation region, thus the carbuncle phenomenon presented in Fig. 2. The computational mesh is purposely generated with some perturbation to the shock, seen in Fig. 2(a) and (b). The carbuncle phenomenon is named first by Peery and Imlay [6] in 1988. It occurs with most upwind schemes, when computing supersonic flow past a blunt body. As Quirk [7] suggested that the insufficient dissipation in the direction parallel to the shock is responsible for the numerical instability. The dissipation required for the numerical stability is mainly introduced by the Riemann solver at the cell interface. With the left and right states across the cell interface, the Riemann solver compromises the two different states, leading to some numerical dissipation [17]. However, in the direction parallel to the shock, the two states across the cell interface are almost the same, which lead to insufficient of dissipation. This will be much more deteriorating, when one family of grid lines is aligned or parallel to the shock.

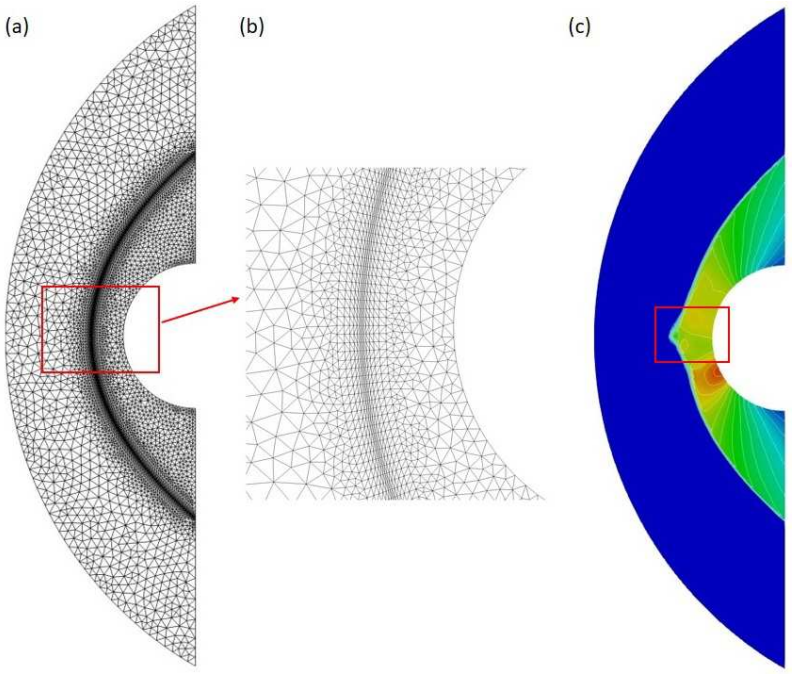

Figure 2: The illustration of mesh adaptation: (a) the computational mesh; (b) close-up view; (c) the carbuncle phenomenon.

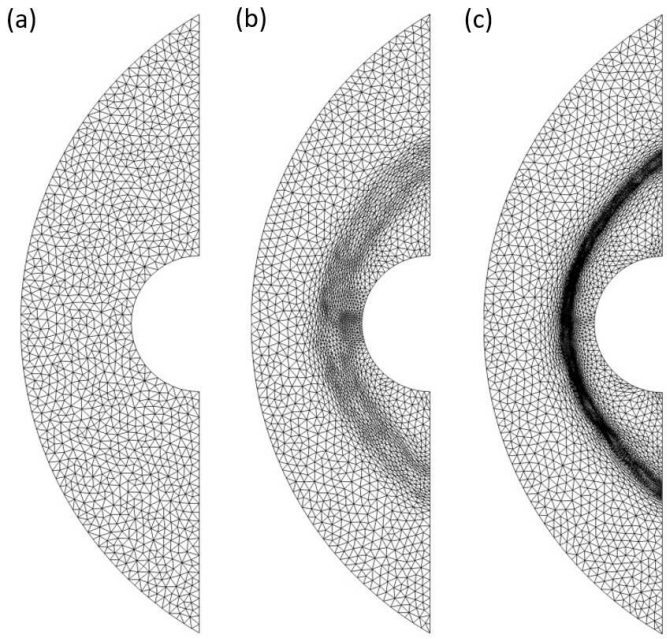

Figure 3: The mesh adaptation for curing the carbuncle phenomenon: (a) the original mesh; (b) first adaptation; (c) second adaptation.

The metrics-based mesh adaptation can locally refine and adjust the anisotropic mesh based on a predefined metric. The original grid is an unstructured grid with very coarse resolution, shown in Fig. 3(a). There are about 2,072 triangular cells in the computational domain. As shown in Fig. 3, the meshes are adapted based on the metric constructed by the Hessian matrix of the pressure field. The total mesh cells of the first and second adaptation are 4,294 and 6,992, respectively. The meshes are well refined within the region of the bow shock. Meanwhile, the adapted anisotropic meshes are elongated in the direction parallel to the shock. This will increase the damping effect in the parallel direction of the shock.

Then, Fig. 4 shows the pressure field computed on different meshes. On the original coarse mesh, the shock is not well resolved with some oscillation in the stagnation regime, shown in Fig. 4(a). In the original ETAU scheme with the multi-dimensional dissipation model, in order to cure the pathological behaviors, the dissipation parameter β may need to increase from the level of 0.001 to 0.01. Here, the numerical results in Fig. 4 are computed without applying the multi-dimensional dissipation model. After two steps of mesh adaptation, the bow shock can be well resolved with the refinement of mesh, shown in Fig. 4(b) and (c). The carbuncle instability is prominently eliminated by the mesh refinement, without applying the multi-dimensional dissipation model. The anisotropic property of the mesh elements across the shock is hard to trigger the instability. The pressure and density profiles along the centerline are plotted in Fig. 5. The black dot line is the pressure profile on the original mesh. The red dash line and blue solid line

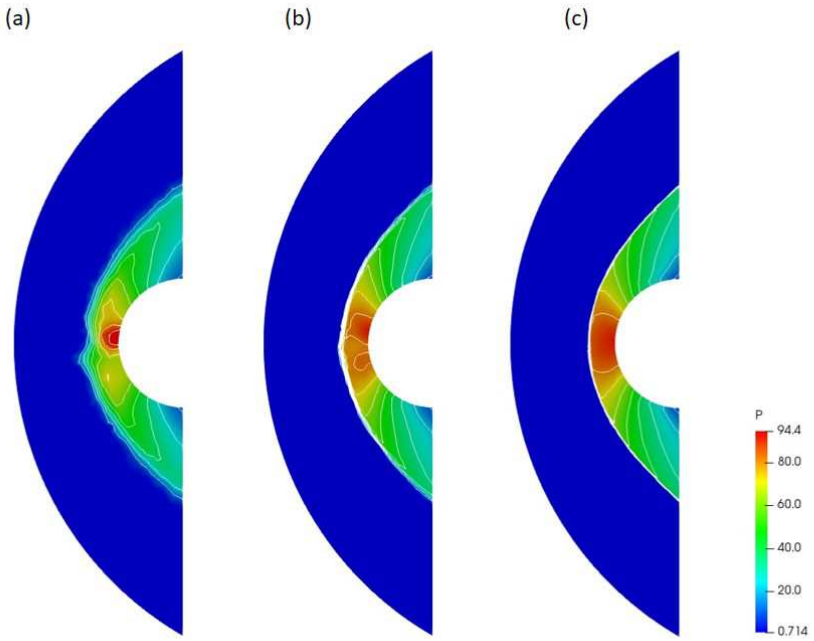

Figure 4: The numerical results of the pressure: (a) the original mesh; (b) first adaptation; (c) second adaptation.

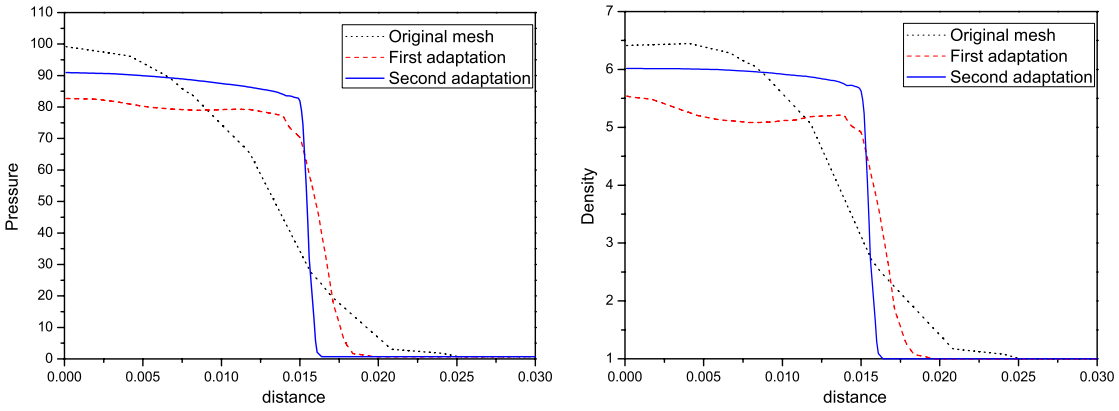

Figure 5: Comparison of the pressure and density profile along the centerline.

are the pressure profiles, calculated from the first and second adaptations, respectively. It is shown that the sharp jump of pressure and density across the bow shock is well resolved after two steps of mesh refinement.

(b) Supersonic flow past a ramp

The second pathological behavior is the kinked Mach stem, when the supersonic flow past a 30° ramp is calculated. A freestream of $Ma=5.5$ is imposed at the inflow boundary

$$(\rho_i,u_i,v_i,p_i)=(5.1489,4.4318,0,25.0893).$$

The matched layer-capturing absorbing boundary condition [39] is applied to the outlet. At the top, bottom and the ramp surface, the slip wall condition is applied.

The original computational mesh is given in Fig. 6(a), with 36,240 triangular cells. Fig. 6(b) is a close-up view of the mesh. This kind of mesh is very common in computation of the supersonic flow past a ramp. The resolution of the grid is quite well. But the alignment of the grid lines with the shock may induce some oscillation of the numerical solution. The reflection of the plane shock from the ramp lies in the double-Mach reflection regime, the principal Mach stem is sometimes kinked, shown in Fig. 7(a). The kinked Mach stem is another famous pathological behavior of upwind schemes. The double reflection shocks are aligned with one family of the grid lines, which is prone to activate the numerical instability. For the original ETAU scheme, when the multi-dimensional dissipation model is applied, the Mach stem can be recovered, shown in Fig. 7(b). Here, the dissipation parameter β is 0.1 to cure the anomaly.

After the mesh adaptation operation, the adapted mesh is presented in Fig. 8, with total cells of 5,468. The mesh is also adapted based on the metric constructed by the Hessian matrix of the pressure field. The cells far away from the shock is coarse, while the cells within the shock region are well resolved. This kind of arrangement can significantly damp the acoustic wave near the inlet and outlet, while the resolution of the shock is remained. The orientation of the cells near the shock is along the parallel direction of the shock. Meanwhile, the shape of the triangular cells is also stretch along the parallel

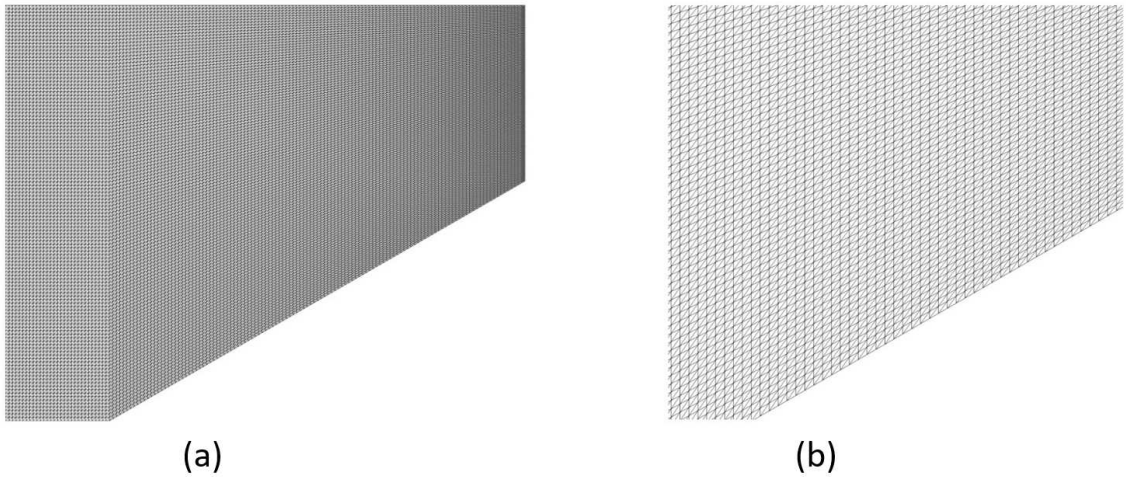

Figure 6: The computational mesh of the Mach stem: (a) the mesh; (b) close-up of the mesh.

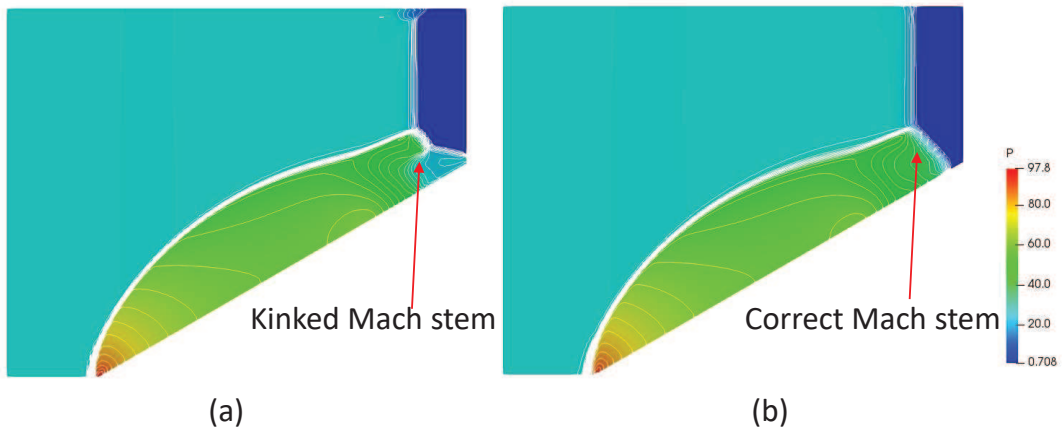

Figure 7: The numerical results: (a) the kinked Mach stem; (b) the correct Mach stem with cure, $\beta=0.1$.

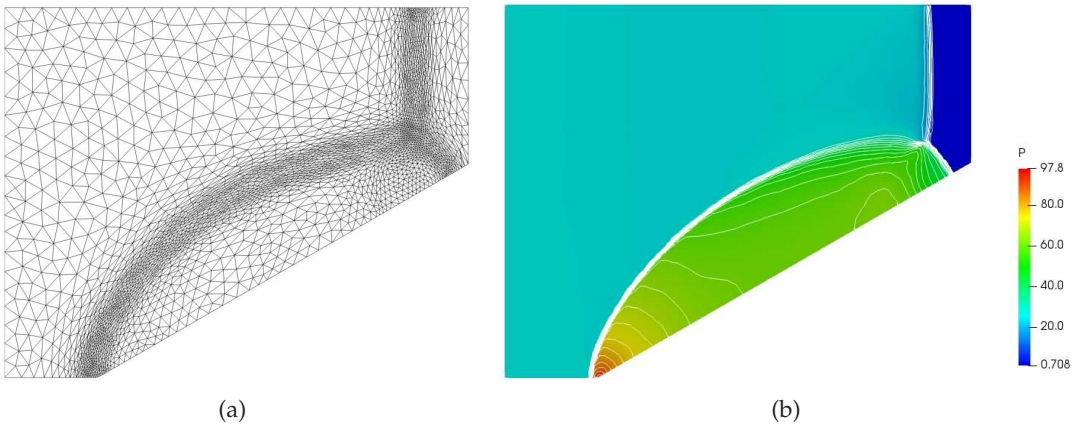

Figure 8: The numerical results: (a) the adapted mesh; (b) the pressure field.

direction. The result is calculated without applying the multi-dimensional dissipation model. The kinked Mach stem is corrected on the adapted anisotropic mesh. This kind of anisotropic mesh is hard to trigger for the instability. Meanwhile, the elongated mesh along the shock has the damping effect to the numerical instability.

(c) Shock wave diffracting around a corner

At the inlet boundary, a free-stream of $Ma=5.09$ is imposed:

$$(\rho_i,u_i,v_i,p_i)=(5.0294,4.0779,0,21.4710).$$

The matched layer-capturing absorbing boundary condition [39] is set at the outlet boundary. The slip wall condition is applied at the top, bottom and along the surface of the corner.

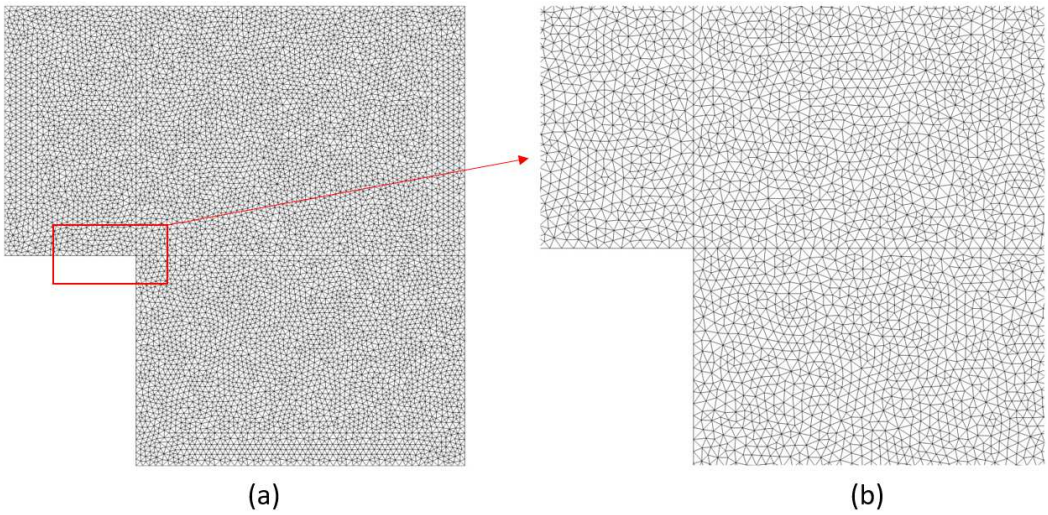

Figure 9: The computational mesh: (a) the original mesh; (b) close-up of the mesh.

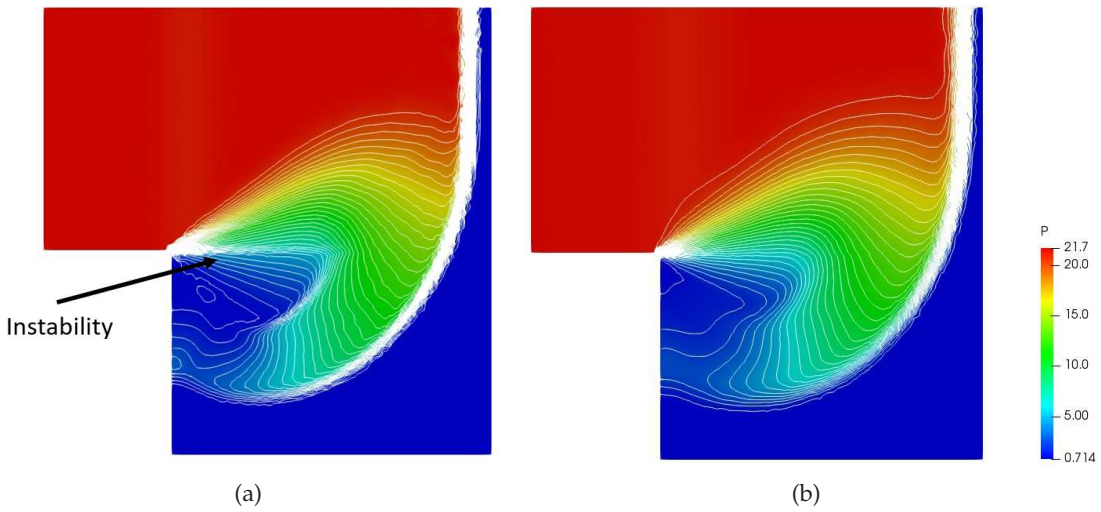

Figure 10: The numerical results of the pressure field: (a) the expansion shock; (b) cure with the multi-dimensional dissipation model, $\beta = 0.001$.

The original mesh contains 14,440 triangles. We purposely generated with some perturbation aligned with the rectangle corner, shown in Fig. 9. As Quirk's observation [7], one family of grid lines aligned to the shock is an essential condition for the activation of the shock instability. The flaw of the original mesh may induce some pathological behaviors of the numerical solution. The instability is observed behind the corner, shown in Fig. 10(a), which is induced by the perturbation of the mesh. In the previous ETAU scheme, after applying the multi-dimensional dissipation model, the instability can be

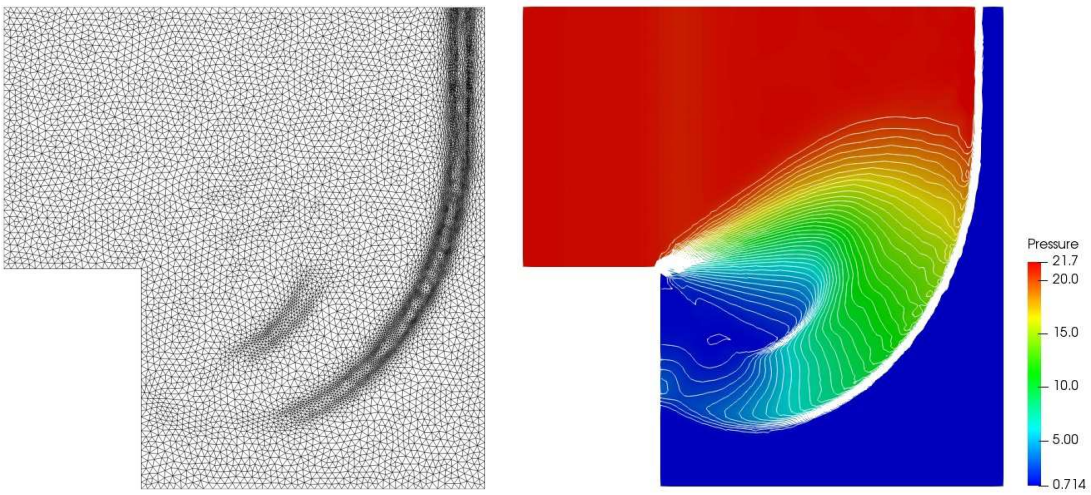

(a) (b)

Figure 11: The numerical result of mesh adaptation.

eliminated. However, when the level of the total numerical dissipation is increased, the rarefaction shock is also smeared, shown in Fig. 10(b).

After the mesh adaptation is applied, the refined mesh is presented in Fig. 11(a). The total number of the triangular cells is 17,379. Here, we applied some operation of the Hessian matrix of the pressure to limit the metric near the corner. Because the cells with large aspect ratio close to the corner may lead to the failure of the numerical solution. The mesh adjustment and refinement during the adaptation process improved the quality of cells around the corner and removed the alignment of grid lines. Without the triggering of the aligned grid line, the expansion shock is alleviated on the refined mesh. Meanwhile, the resolution of the rarefaction shock and the strong shock are well improved, due to the refinement of the adapted anisotropic mesh, shown in Fig. 11(b). With the mesh adaptation procedure, the rarefaction shock is maintained.

To show the mesh adaptation procedure of the unsteady process, the movement of the shock wave is presented in Fig. 12 at three snapshots. The adapted meshes are presented in Fig. 12(a), (b) and (c), while the corresponding pressure fields are presented in Fig. 12(d), (e) and (f). The positions of the shock wave are well captured by the refined meshes. Meanwhile, the shock wave are stable and clear with the mesh adaption.

5 Conclusions

In conclusion, a metric-based mesh adaptation algorithm is applied for curing the pathological behaviors of the original upwind finite volume scheme. The basic flow solver applied is the enhanced time-accurate upwind (ETAU) scheme. In the original ETAU

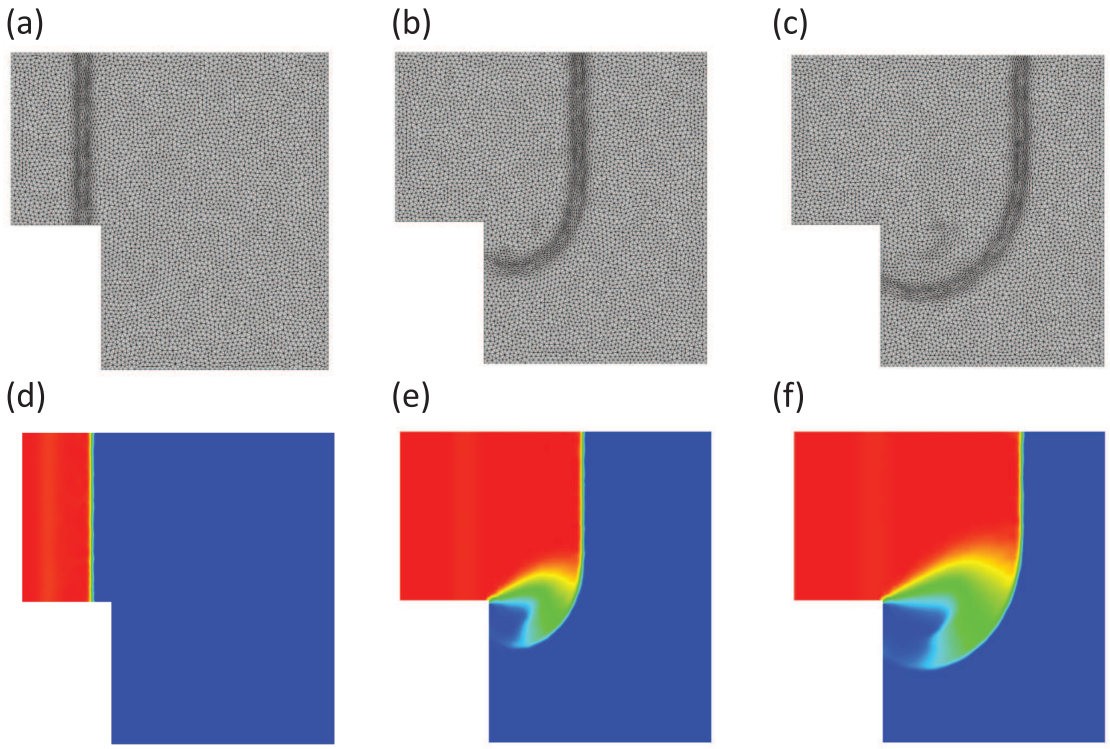

Figure 12: The unsteady evolution of the shock.

scheme, the multi-dimensional dissipation model is required to cure the pathological behaviors of upwind schemes. In present work, the mesh adaption strategy provides an alternative way to cure the pathological behaviors of the upwind schemes. The Hessian-based metric can not only improve the resolution across the shock, but also has the effect of elongating the edges of cells parallel to the shock. The stretch of the cells along the parallel direction of shock increases the dissipation in this direction. This is beneficial for the damping of the numerical instability. Several classic numerical tests show that the mesh adaptation has the beneficial effect to alleviate the pathological behaviors, due to the anisotropic property of the mesh and the improved resolution across the shock. The flaws of upwind schemes have complicate origin. This work is a tentative effort to confront this issue. More works still remained to find out the numerical and physical explanation of the pathological behaviors of Godunov type upwind schemes.

Acknowledgments

The authors gratefully acknowledge the financial support received from the National Natural Science Foundation of China, under Grant No. 91841302 and No. 51976184, the Basic Science Center Program for Multiphase Evolution in Hypergravity of the National

Natural Science Foundation of China (No. 51988101) and the Fundamental Research Funds for the Central Universities (No. 2019QNA4034).

References

[1] S.K. Godunov, Finite difference method for numerical computation of discontinuous solutions of the equations of fluid dynamics. Mat. Sb., 47 (1959), 271-306.
[2] P.L. Roe, Approximate Riemann solvers, parameter vectors, and difference schemes, J. Comput. Phys., 43 (1981), 357-372.
[3] S. Osher and S. Chakravarthy, Upwind schemes and boundary conditions with applications to euler euqations in general geometries. J. Comput. Phys., 50 (1983), 447-481.
[4] B. Einfeldt, On Godunov-type methods for gas dynamics, SIAM J. Numer. Anal., 25 (1988), 294318.
[5] J.S. Shang and E. Josyula, Numerical simulations of non-equilibrium hypersonic flow past blunt bodies, AIAA paper 88-0512, 1988.
[6] K.M. Peery and S.T. Imlay, Blunt-body flow simulations, AIAA paper 88-2904, 1988.
[7] J.J. Quirk, A contribution to the great Riemann solver debate, Int. J. Numer. Meth. Fl., 18 (1994), 555-574.
[8] R. Sanders, E. Morano and M.C. Druguet, Multidimensional dissipation for upwind schemes: Stability and applications to gas dynamics, J. Comput. Phys., 145 (1998), 511-537.
[9] J.C. Robinet, J. Gressier, G. Casalis and J.M. Moschetta, Shock wave instability and carbuncle phenomenon: Same intrinsic origin?, J. Fluid Mech., 417 (2000), 237263.
[10] J. Gressier and J.M. Moschetta, Robustness versus accuracy in shock-wave computations, Int. J. Numer. Meth. Fl., 33 (2000), 313-332.
[11] M. Dumbser, J.M. Moschetta and J. Gressier, A matrix stability analysis of the carbuncle phenomenon, J. Comput. Phys., 197 (2004), 647-670.
[12] K. Xu and J. Hu, Projection dynamics in Godunov-type schemes, J. Comput. Phys., 142 (1998), 412-427.
[13] K. Xu and Z. Li, Dissipative mechanism in Godunov-type schemes, Int. J. Numer. Meth. Fluids, 37 (2001), 1-22.
[14] F. Kemm, Heuristical and numerical considerations for the carbuncle phenomenon, Appl. Math. Comput., 320 (2018), 596-613.
[15] H.C. Lin, Dissipation additions to flux difference splitting, J. Comput. Phys., 117 (1995), 20-27.
[16] S.S Kim, C. Kim, O. Rho, S.K. Hong, Cures for the shock instability: Development of a shock-stable Roe scheme, J. Comput. Phys., 185 (2003), 342-374.
[17] C.Y. Loh and P.C. Jorgenson, Multi-dimensional dissipation for cure of pathological behaviors of upwind scheme, J. Comput. Phys., 228 (2009), 1343-1346.
[18] N. Fleischmann, S. Adami, X.Y. Hu and N. Adams, A low dissipation method to cure the grid-aligned shock instability, J. Comput. Phys., 401 (2020), 109004.
[19] N. Fleischmann, S. Adami and N. Adams, A shock-stable modification of the HLLC Riemann solver with reduced numerical dissipation, J. Comput. Phys., 423 (2020), 109762.
[20] M. Pandolfi and D. D'Ambrosio, Numerical instabilities in upwind methods: Analysis and cures for the "carbuncle" phenomenon, J. Comput. Phys., 166 (2001), 271-301.
[21] A.V. Rodionov, Artificial viscosity in Godunov-type schemes to cure the carbuncle phenomenon, J. Comput. Phys., 345 (2017), 308-329.

[22] R. Lohner, Adaptive remeshing for transient problems, Comput. Methods Appl. Mech. Engrg., 75 (1989), 195-214.
[23] J. Peraire, J. Peiro and K. Morgan, Adaptive remeshing for three-dimensional compressible flow computations, J. Comput. Phys., 103 (1992), 69-85.
[24] O. Zienkiewicz and J. Wu, Automatic directional refinement in adaptive analysis of compressible flows, Int. J. Numer. Meth. Engng., 37 (1994), 198-210.
[25] M.J. Castro-Diaz, F. Hecht, B. Mohammadi and O. Pironneau, Anisotropic unstructured mesh adaptation for flow simulations, Int. J. Numer. Meth. Fl., 25 (1997) 475-491.
[26] F. Hecht and B. Mohammadi, Mesh adaptation by metric control for multi-scale phenomena and turbulence, AIAA paper 97-0859, 1997.
[27] W. Hassan and M. Picasso, An anisotropic adaptive finite element algorithm for transonic viscous flows around a wing, 111 (2015), 33-45.
[28] C.Y. Loh and P.C. Jorgenson, A time-accurate upwind unstructured finite volume method for compressible flow with cure of pathological behaviors, Proceedings of 18th AIAA Computational Fluid Dynamics Conference, AIAA-2007-4463, June 25-28, Miami, Florida, USA, 2007.
[29] C.Y. Loh and P.C. Jorgenson, Nearly all-speed, stabilized time-accurate upwind scheme on unstructured grid, AIAA J., 48 (2010), 644-653.
[30] Y. Xia, G. Wang, Y. Zheng, T. Ji and C.Y. Loh, Incorporation of NURBS boundary representation with an unstructured finite volume approximation, Commun. Comput. Phys., 24 (2018), 791-809.
[31] G.D. van Albada, B. van Leer and W.W. Jr. Roberts, A comparative study of computational methods in cosmic gas dynamics, Astron. Astrophys., 108 (1982), 76-84.
[32] H. Nessyahu and E. Tadmor, Non-oscillatory central differencing for hyperbolic conservation laws, J. Comput. Phys., 87 (1990), 408-463.
[33] S.-C. Chang, X.-Y. Wang, C.-Y. Chow, The method of space-time conservation element and solution element–A new approach for solving the Navier-Stokes and Euler equations, J. Comput. Phys., 119 (1995), 295-324.
[34] P.J. Frey and F. Alauzet, Anisotropic mesh adaptation for CFD computations, Comput. Methods Appl. Mech. Engrg., 194 (2005), 5068-5082.
[35] C. Dobrzynski and P. Frey, Anisotropic Delaunay mesh adaptation for unsteady simulations, in: R.V. Garimella (ed.), Proceedings of the 17th International Meshing Roundtable, 2008, 177-194.
[36] C. Dapogny, C. Dobrzynski and P. Frey, Three-dimensional adaptive domain remeshing, implicit domain meshing, and applications to free and moving boundary problems, J. Comput. Phys., 262 (2014), 358378
[37] A. Loseille, Handbook of Numerical Analysis: Chapter 10 – Unstructured mesh generation and adaption. Volume 18, Elsevier 2017, 263-302.
[38] Y.V. Vassilevski, V.G. Dyadechko and K.N. Lipnikov, Hessian-based anisotropic mesh adaptation in domains with boundaries, Russ. J. Numer. Amal. Math. Modelling, 20 (2005), 391-402.
[39] C.Y. Loh, Application of new absorbing boundary condition with finite volume schemes, AIAA J., 54 (2017), 1591-1602.